Dynamical characteristics of honeycomb two-dimensional gyroscopic metamaterials

Ji-Hou Yang,[*] Yi-Bo Wang,[†] and Xiao-Dong Yang[‡]

Faculty of Materials and Manufacturing, Beijing University of Technology, Beijing 100124, China
and Beijing Key Laboratory of Nonlinear Vibrations and Strength of Mechanical Structures, Beijing 100124, China

Suppression of noise and vibration suppression is important in various fields, such as the living environment, industrial development, and national defense and security. The bandgap properties of phononic crystal metamaterials provide an approach for controlling and eliminating harmful vibrations in equipment and noise in the environment. In this study, we used two types of two-dimensional honeycomb gyroscopic metamaterials: free and constrained. The dynamic equations of the two systems were established using angular momentum and Lagrange theorems. The dispersion relations of the two systems were obtained based on the Bloch theorem, and the influence of the gyroscope angular momentum or gyroscope speed on the dispersion relations was analyzed. Numerical simulations were conducted to analyze the wave propagation characteristics and polarization under different excitation conditions in a limited space for both types of metamaterial structures. The constrained-type and free-type metamaterials were compared, and the regularities of the dispersion relations and wave propagation characteristics by the gyroscope effect were summarized. This study provided a comprehensive and in-depth understanding of the bandgap and wave propagation properties of gyroscopic metamaterials and provided ideas for the design of bandgap modulation in metamaterials.

I. INTRODUCTION

Vibrations and noise can cause significant harm in various fields, such as industrial engineering and daily life, causing equipment damage, decreased production efficiency, reduced machine precision, and compromised health and quality of life for residents. Therefore, the suppression of noise and vibrations is significantly important. Phononic crystal metamaterials, a type of metamaterials for sound and vibration propagation and control, have gained widespread attention [1–4]. Phononic crystal metamaterials are composite materials composed of periodic arrangements of unit structures in space [5,6]. They have been proposed as a physical concept for elastic waves in the field of condensed matter physics based on research on photonic crystals [7]. Owing to their dispersive properties, waves within the passband can propagate, whereas waves within the stopband are suppressed [8–11].

The concept of phononic crystals was derived from photonic crystals; however, research on phononic crystals is largely based on the theory of elastic wave propagation in periodic structures. Li and Chan [12] first proposed the concept of acoustic metamaterials and studied a solid–liquid phononic crystal composed of soft silicone rubber and water. They found that the effective mass density and effective bulk modulus were both negative within a certain frequency range. Pai *et al.* [13] designed a type of multiresonant phononic metamaterial beam. Because of the damping effect,

the bandgaps formed by the two subsystems were connected to form a wider bandgap, which was validated through numerical simulations. Yang *et al.* [14] studied the longitudinal waves of one-dimensional spring-mass systems under transverse periodic vibrations. They used high-frequency vibrations as parameter excitation to provide pseudo-stiffness and realized the tuning of bandgaps in a structure using parameter excitation.

Research on gyroscopes covers a certain proportion of the field of dynamics and control [15–17]. The frequency mode of the structure can be changed by introducing gyroscope rotors [18–20]. The addition of gyroscopic rotors to phononic crystal metamaterials can change and control their dispersion properties [21,22], thus suppressing vibrations and noise in a certain frequency range, as expected. In addition, using an appropriate gyro-phononic crystal structure, special materials and structures can be designed, such as wave polarizers, filters, wave accelerators, decelerators, and waveguides with specified directions [23–25].

Brun *et al.* [26] proposed the first gyro-elastic lattice. Through a combination of simulations and theory, they demonstrated that gyroscopic properties could be used for the construction of shielding cloaks around obstacles, enabling waves to propagate around them. Zhou and Zhao [27] extended the observed unidirectional wave properties in discrete lattice structures to study gyroscopic continua. They established a surface equation for acoustic gyroscopic continua using the Hermite mass density tensor in continuum mechanics to explain the generation of unidirectional waves. Wang *et al.* [28] and Nash *et al.* [29] studied a gyroscopic structure arranged in a hexagonal pattern and found that waves with frequencies within the bandgap range ex-

[*]jjihouyang@163.com
[†]yibowang1102@163.com
[‡]Corresponding author: jxdyang@163.com

hibit unidirectional propagation in the structure. Hexagonal phonon crystals are highly symmetrical structures that can be bisected into two identical halves by any of their diagonals. This uniformity ensures consistent acoustic wave propagation, regardless of the entry direction of sound waves, making it particularly advantageous for sound wave control applications. Furthermore, the high symmetry of these hexagonal phonon crystals triggers strong Bragg scattering in multiple directions, resulting in a broader bandgap than other phononic crystals.

Brun's use of gyroscopes for dynamic control of phononic crystal metamaterials has opened research directions. Modeling methods and established dynamic equations have been widely adopted by several scholars. However, the established equations only reflect the influence of gyroscope rotor inertia and height and do not consider key factors such as rotation speed. The obtained dispersion relationship is inaccurate and cannot be used to obtain the bandgaps, limiting the research scope of gyroscope control. In addition, relatively few studies have been conducted on the polarization properties of waves in gyroscopic metamaterials. Summarizing the wave laws for gyroscopic metamaterials can further enhance wave control functionality.

In view of the above-mentioned problems, this study conducted the following research. Section II presents the derivation of the motion equations for two types of gyroscopic metamaterials using the angular momentum and Lagrange theorems, and the dispersion relationships were obtained based on the Bloch theorem. Section III analyzes the influence of the gyroscope's angular momentum and spring dimensions on the dispersion relationships, respectively, and verifies the structural bandgap through numerical simulations, and finally discusses the magnitude and direction of the group velocities corresponding to different dispersion surfaces. Section IV analyzes the wave propagation and polarization characteristics of the two types of metamaterial structures under different excitation conditions in a finite space through numerical simulations. Section V summarizes the study and presents the conclusions drawn from this study.

II. MODELING

Research on gyroscopic dynamics has shown that the rotation of the gyros causes a bifurcation of the inherent frequency of the structure and changes the mode of the structure, which leads to ideas for the dynamic regulation of metamaterials. The effect of changing the dispersion relationships of the systems can be achieved by introducing gyroscopes into metamaterials, thereby providing a method for controlling acoustic vibrations. Two metamaterial models were proposed in this study: honeycomb-constrained and honeycomb-free gyroscopic metamaterials. Based on the Lagrange equations and momentum moment theorem, the dynamic equations for the two types of metamaterials were obtained by analyzing the cell structure.

A. Free-type gyroscopic metamaterials

First, dynamic modeling was performed for a two-dimensional (2D) honeycomb-type free gyrometamaterial. As shown in Fig. 1(a), the gyro units are connected by springs to form a gyrometamaterial with the basic structure of a regular hexagon. In this model, it was assumed that the springs provide only torque and not horizontal tension. Therefore, only the overall torsion angle of the gyro and framework were considered, and the horizontal displacement was not considered. The rotation angle of the framework around the x axis is θ, and the rotation angle around the y axis is φ. The positive direction of the coordinate axis is defined as positive for rotation. According to crystallographic theory, a 2D regular hexagonal lattice is a complex lattice that includes two types of lattice points with different geometric environments. Figure 1(b) shows two types of gyro units with some differences owing to their different spring-connection modes.

As shown in Fig. 1(c), the difference in the direction of the force applied by the springs around the lattice points leads to the fact that the geometrical environments of the lattice points in the structure are not all the same, and as a result we define two types of lattice points: u-lattice points and v-lattice points. Then, the torques acting on the two types of gyroscopic units along the x and y axes in the (m, n) basic unit, in the mth row and nth column, are

$$M_x^u = c_1\left(\theta_{m,n}^v - \theta_{m,n}^u\right) + \frac{1}{4}c_1\left(\theta_{m-1,n}^v - \theta_{m,n}^u\right) + \frac{1}{4}c_1\left(\theta_{m,n-1}^v - \theta_{m,n}^u\right) + \frac{\sqrt{3}}{4}c_1\left(\varphi_{m-1,n}^v - \varphi_{m,n}^u\right) + \frac{\sqrt{3}}{4}c_1\left(\varphi_{m,n-1}^v - \varphi_{m,n}^u\right)$$
$$+ \frac{3}{4}c_2\left(\theta_{m-1,n}^v - \theta_{m,n}^u\right) + \frac{3}{4}c_2\left(\theta_{m,n-1}^v - \theta_{m,n}^u\right) + \frac{\sqrt{3}}{4}c_2\left(\varphi_{m-1,n}^v - \varphi_{m,n}^u\right) + \frac{\sqrt{3}}{4}c_2\left(\varphi_{m,n-1}^v - \varphi_{m,n}^u\right) + H\dot{\varphi}_{m,n}^u, \tag{1}$$

$$M_y^u = \frac{3}{4}c_1\left(\varphi_{m-1,n}^v - \varphi_{m,n}^u\right) + \frac{3}{4}c_1\left(\varphi_{m,n-1}^v - \varphi_{m,n}^u\right) + \frac{\sqrt{3}}{4}c_1\left(\theta_{m-1,n}^v - \theta_{m,n}^u\right) + \frac{\sqrt{3}}{4}c_1\left(\theta_{m,n-1}^v - \theta_{m,n}^u\right) + c_2\left(\varphi_{m,n}^v - \varphi_{m,n}^u\right)$$
$$+ \frac{1}{4}c_2\left(\varphi_{m-1,n}^v - \varphi_{m,n}^u\right) + \frac{1}{4}c_2\left(\varphi_{m,n-1}^v - \varphi_{m,n}^u\right) + \frac{\sqrt{3}}{4}c_2\left(\theta_{m-1,n}^v - \theta_{m,n}^u\right) + \frac{\sqrt{3}}{4}c_2\left(\theta_{m,n-1}^v - \theta_{m,n}^u\right) - H\dot{\theta}_{m,n}^u, \tag{2}$$

$$M_x^v = c_1\left(\theta_{m,n}^u - \theta_{m,n}^v\right) + \frac{1}{4}c_1\left(\theta_{m+1,n}^u - \theta_{m,n}^v\right) + \frac{1}{4}c_1\left(\theta_{m,n+1}^u - \theta_{m,n}^v\right) + \frac{\sqrt{3}}{4}c_1\left(\varphi_{m+1,n}^u - \varphi_{m,n}^v\right) + \frac{\sqrt{3}}{4}c_1\left(\varphi_{m,n+1}^u - \varphi_{m,n}^v\right)$$
$$+ \frac{3}{4}c_2\left(\theta_{m+1,n}^u - \theta_{m,n}^v\right) + \frac{3}{4}c_2\left(\theta_{m,n+1}^u - \theta_{m,n}^v\right) + \frac{\sqrt{3}}{4}c_2\left(\varphi_{m+1,n}^u - \varphi_{m,n}^v\right) + \frac{\sqrt{3}}{4}c_2\left(\varphi_{m,n+1}^u - \varphi_{m,n}^v\right) + H\dot{\varphi}_{m,n}^v, \tag{3}$$

$$M_y^v = \frac{3}{4}c_1\left(\varphi_{m+1,n}^u - \varphi_{m,n}^v\right) + \frac{3}{4}c_1\left(\varphi_{m,n+1}^u - \varphi_{m,n}^v\right) + \frac{\sqrt{3}}{4}c_1\left(\theta_{m+1,n}^u - \theta_{m,n}^v\right) + \frac{\sqrt{3}}{4}c_1\left(\theta_{m,n+1}^u - \theta_{m,n}^v\right) + c_2\left(\varphi_{m,n}^u - \varphi_{m,n}^v\right)$$

$$+ \frac{1}{4}c_2\left(\varphi_{m+1,n}^u - \varphi_{m,n}^v\right) + \frac{1}{4}c_2\left(\varphi_{m,n+1}^u - \varphi_{m,n}^v\right) + \frac{\sqrt{3}}{4}c_2\left(\theta_{m+1,n}^u - \theta_{m,n}^v\right) + \frac{\sqrt{3}}{4}c_2\left(\theta_{m,n+1}^u - \theta_{m,n}^v\right) - H\dot{\theta}_{m,n}^v, \tag{4}$$

where c_1 is the transverse torsion stiffness of the spring, c_2 is the longitudinal torsion stiffness of the spring, $H = I_z\Omega$ is the angular momentum of the gyroscope, I_z is the moment of inertia of the gyroscope relative to the axis of rotation, and Ω is the rotational speed of the gyroscope.

Based on the angular momentum theorem, the kinematic equations for the two types of gyroscope units in the (m, n) cell are as follows:

$$I\ddot{\theta}_{m,n}^u = M_x^u, \quad I\ddot{\varphi}_{m,n}^u = M_y^u, \quad I\ddot{\theta}_{m,n}^v = M_x^v, \quad I\ddot{\varphi}_{m,n}^v = M_y^v, \tag{5}$$

where I is the moment of inertia of the gyro with respect to the x and y axes.

Assuming that the in-plane displacement of each gyroscope in the lattice is harmonic and solving the above equation based on the Bloch theorem, the solution can be assumed to have the following form:

$$\theta_{m,n}^u = Ae^{i\mathbf{k}\cdot\mathbf{T}(m,n)^T}e^{i\omega t}, \varphi_{m,n}^u = Be^{i\mathbf{k}\cdot\mathbf{T}(m,n)^T}e^{i\omega t},$$

$$\theta_{m,n}^v = Ce^{i\mathbf{k}\cdot\mathbf{T}(m,n)^T}e^{i\omega t}, \varphi_{m,n}^v = De^{i\mathbf{k}\cdot\mathbf{T}(m,n)^T}e^{i\omega t}, \tag{6}$$

where A, B, C, and D are amplitudes; $\mathbf{k} = (k_1, k_2)^T$ is the planar wave vector, where k_1 is the wave number along the x axis and k_2 is the wave number along the y axis; and $\mathbf{T} = (\mathbf{t}_1, \mathbf{t}_2)$ is the basis vector matrix, where $\mathbf{t}_1$ and $\mathbf{t}_2$ are as shown in Fig. 1(c).

Substituting Eq. (6) into Eq. (5), we obtain the following dispersion equation:

$$\mathbf{N}\begin{pmatrix} A \\ B \\ C \\ D \end{pmatrix} = \begin{pmatrix} 0 \\ 0 \\ 0 \\ 0 \end{pmatrix}, \tag{7}$$

and the explicit expression of the matrix $\mathbf{N}$ is provided in Appendix A.

Based on the criterion for the existence of nontrivial solutions in the system, the dispersion relation of the system can be further derived as

$$\det(\mathbf{N}) = 0. \tag{8}$$

When considering various values of the wave vector $\mathbf{k}$, it was observed that the equation had a trivial solution $\omega = 0$, which corresponded to the rigid-body motion of the system constrained by static conditions. In addition to the trivial solution, three positive real solutions also existed, indicating that the two-dimensional honeycomb gyrometamaterial system featured three dispersion surfaces. The dispersion characteristics of the system are explored in detail in the following sections.

B. Constrained-type gyroscopic metamaterials

The two-dimensional honeycomb-constrained gyroscopic metamaterial is shown in Fig. 2(a). The translational motion of the particle in the Oxy plane caused nutation of the gyro. The nutation angle of the gyro could be regarded as a small quantity in the calculation because the particle's motion range was small compared to the gyro height. In this study, the motion amplitude of a particle in the z direction was negligible.

To obtain the dynamic equation of the periodic structure, the Lagrange equation was used to analyze the unit structure, as shown in Fig. 2(b). The unit consisted of a gyroscope and a particle. The plane motion of the mass point is described by Cartesian coordinates x and y, whereas the motion of the gyroscope is described by Euler angles γ, ϕ, and ψ, and the transformation relationship between the two coordinates is as follows:

$$x = h\sin\gamma\cos\phi, y = h\sin\gamma\sin\phi, \tag{9}$$

where h is the height of the gyro. The Lagrange multiplier of the unit structure is expressed as

$$L = \tfrac{1}{2}I_1\Omega_1^2 + \tfrac{1}{2}I_2\Omega_2^2 + \tfrac{1}{2}I_3\Omega_3^2 + \tfrac{1}{2}m(\dot{x}^2 + \dot{y}^2) - V, \tag{10}$$
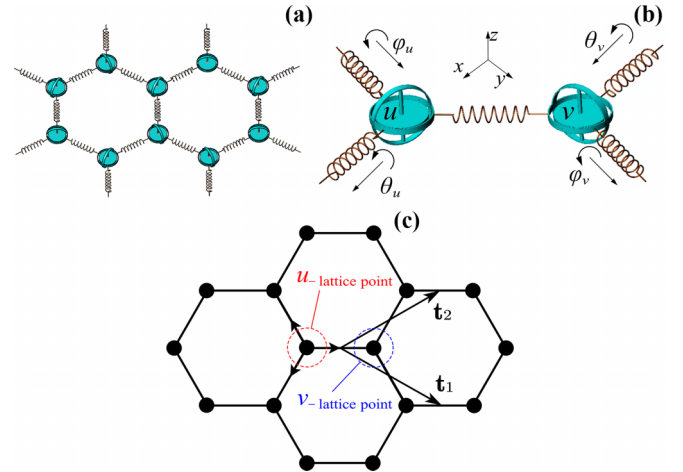

FIG. 1. (a) Model of gyroscopic metamaterials. The unit structure of a metamaterial is composed of a single gyroscope and an external framework. The external framework is connected by springs and arranged in a regular hexagonal plane. (b) Periodic unit. θ_u represents the angle of rotation around the x axis for u-lattice points, φ_u represents the angle of rotation around the y axis for u-lattice points, θ_v represents the angle of rotation around the x axis for v-lattice points, and φ_v represents the angle of rotation around the y axis for v-lattice points. (c) Honeycomb lattice periodicity. $\mathbf{t}_1 = (3l/2, -\sqrt{3}l/3)^T$ and $\mathbf{t}_2 = (3l/2, \sqrt{3}l/3)^T$ are the basis vectors for the periodic lattice, where l is the lattice length.
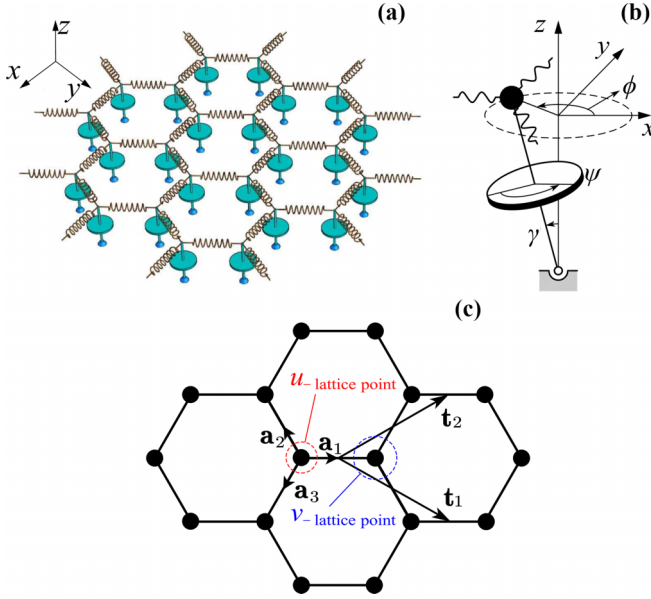
FIG. 2. (a) Model of gyroscopic metamaterials. The particle with mass m and the gyro structure shown below formed the metamaterial cell, which was connected by a spring of stiffness c, forming a gyroscopic metamaterial with a two-dimensional planar lattice in the shape of a honeycomb. It should be noted that the bottom of the gyroscope was hinged and fixed. (b) Unit structure diagram. γ, ϕ, and ψ are nutation, precession, and rotation angles, respectively. (c) Honeycomb lattice periodicity. $\mathbf{a}_1 = (1, 0)^T$, $\mathbf{a}_2 = (-1/2, \sqrt{3}/2)^T$, and $\mathbf{a}_3 = (-1/2, -\sqrt{3}/2)^T$ were used to define the direction of elastic force.

where I_1, I_2, and I_3 ($I_1 = I_2$) are the moments of inertia, and Ω_i ($i = 1, 2,$ and 3) is the angular velocity of the gyro, expressed as

$$\Omega_1 = \dot{\gamma}, \quad \Omega_2 = \dot{\phi} \sin \gamma, \quad \Omega_3 = \dot{\psi} + \dot{\phi} \cos \gamma. \quad (11)$$

The Lagrange operator in the form of the Euler angles was obtained by substituting Eqs. (9) and (11) into Eq. (10), depending on the Lagrange equations used for the three Euler angles.

$$\frac{d}{dt}[I_3(\dot{\psi} + \dot{\phi} \cos \gamma)] = 0, \quad (12)$$

$$I_1(\ddot{\gamma} - \cos \gamma \sin \gamma \dot{\phi}^2) + I_3 \Omega \sin \gamma \dot{\phi}$$

$$+ mh^2 \cos \gamma [\cos \gamma \ddot{\gamma} - \sin \gamma (\dot{\gamma}^2 + \dot{\phi}^2)] + \frac{\partial V}{\partial \gamma} = 0, \quad (13)$$

$$I_1 \sin \gamma (\sin \gamma \ddot{\phi} + 2 \cos \gamma \dot{\phi} \dot{\gamma}) - I_3 \Omega \sin \gamma \dot{\gamma}$$

$$+ mh^2 \sin \gamma (2 \cos \gamma \dot{\phi} \dot{\gamma} + \sin \gamma \ddot{\phi}) + \frac{\partial V}{\partial \phi} = 0. \quad (14)$$

Using Eq. (12), we obtained the rotational speed of the gyro $\Omega = \dot{\psi} + \dot{\phi} \cos \gamma$.

To unify the variables, the coordinate transformations in Eqs. (13) and (14) were applied using Eq. (9) to obtain the

dynamics equations of the unit structure

$$\left(m + \frac{I_1}{h^2}\right)\ddot{x} + \frac{I_3}{h^2}\Omega\dot{y} + \frac{\partial V}{\partial x}$$

$$= 0, \left(m + \frac{I_1}{h^2}\right)\ddot{y} - \frac{I_3}{h^2}\Omega\dot{x} + \frac{\partial V}{\partial y} = 0. \quad (15)$$

It was observed that the gyroscope introduced an additional mass I_1/h^2 to the system and a gyroscope term $\pm\Omega I_3/h^2$, where the presence of $\pm\Omega I_3/h^2$ caused coupling of the x- and y-direction motions of the particle, resulting in particle polarization motion.

Using this equation, we derived the dynamic equation of a periodic structure containing two types of lattice points, as shown in Fig. 2(c), which considers the specific form of the elastic force.

$$M\ddot{\mathbf{U}}_{m,n} + G\mathbf{R}\dot{\mathbf{U}}_{m,n} - c[\mathbf{a}_1 \cdot (\mathbf{V}_{m,n} - \mathbf{U}_{m,n})\mathbf{a}_1 + \mathbf{a}_2$$

$$\cdot (\mathbf{V}_{m-1,n} - \mathbf{U}_{m,n})\mathbf{a}_2 + \mathbf{a}_3 \cdot (\mathbf{V}_{m,n-1} - \mathbf{U}_{m,n})\mathbf{a}_3]$$

$$= 0, M\ddot{\mathbf{V}}_{m,n} + G\mathbf{R}\dot{\mathbf{V}}_{m,n} - c[\mathbf{a}_1 \cdot (\mathbf{U}_{m,n} - \mathbf{V}_{m,n})\mathbf{a}_1 + \mathbf{a}_2$$

$$\cdot (\mathbf{U}_{m+1,n} - \mathbf{V}_{m,n})\mathbf{a}_2 + \mathbf{a}_3 \cdot (\mathbf{U}_{m,n+1} - \mathbf{V}_{m,n})\mathbf{a}_3] = 0,$$

$$(16)$$

where $\mathbf{U} = [x, y]^T$ and $\mathbf{V} = [x, y]^T$ denote the displacement vectors of the two types of gyroscopic units, $M = m + I_1/h^2$ represents the equivalent mass of the particle, and $G = I_3\Omega/h^2$ is the gyroscope constant, whose magnitude reflects the gyroscope rotation speed. The sign of G indicates the direction of the gyroscope rotation. The square matrix $\mathbf{R} = [0, 1; -1, 0]$ is antisymmetric, and c is the spring stiffness coefficient.

According to Bloch theory for 2D periodic lattices, the displacement solution for the (m, n)th unit structure can be assumed as follows:

$$\mathbf{U}_{m,n} = \mathbf{u}^{(0)}e^{i\mathbf{k}\cdot\mathbf{T}(m,n)^T}e^{i\omega t}, \mathbf{V}_{m,n} = \mathbf{v}^{(0)}e^{i\mathbf{k}\cdot\mathbf{T}(m,n)^T}e^{i\omega t}, \quad (17)$$

where $\mathbf{u}^{(0)}$ and $\mathbf{v}^{(0)}$ are the amplitudes of the initial unit cell. Substituting Eq. (17) into Eq. (16) yields the dispersion relation of the 2D honeycomb gyroid metamaterial.

$$\det(\omega^2\mathbf{M} + \omega\mathbf{G} - \mathbf{C}) = 0. \quad (18)$$

The specific forms of $\mathbf{M}$, $\mathbf{G}$, and $\mathbf{C}$ are found in Appendix B.

III. DISPERSION ANALYSIS

Dispersion analysis is a crucial technique for understanding the behavior of electromagnetic and acoustic waves in metamaterials. Researchers can gain insights into the dispersion properties of the materials and design materials with unique electromagnetic or acoustic properties by analyzing the wave vector, frequency, and phase velocity of waves passing through the material.

A. Dispersion relationship

Dispersion analysis of metamaterials generally includes the analysis of dispersion relations and group velocities. The dispersion relations describe the relationships between the wave vector and the frequency in the metamaterial. Through analysis of the dispersion relations, researchers can determine
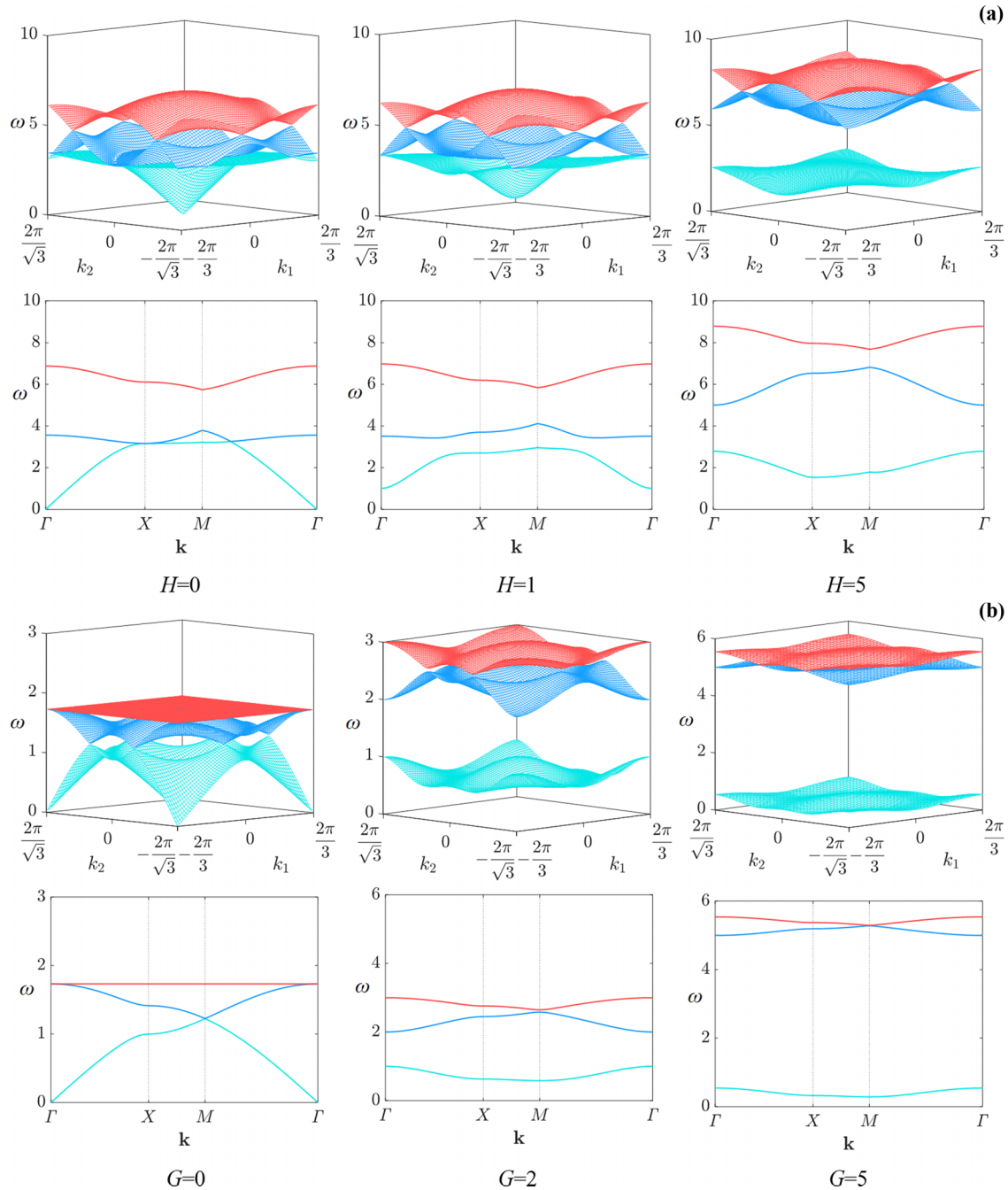
FIG. 3. Dispersion surfaces and curves. (a) and (b) describe the dispersion relationships of free and constrained honeycomb metamaterials, respectively.

the key properties of a metamaterial, such as its refractive index, which affects the direction and speed of electromagnetic or acoustic waves passing through the material. Dispersion relations can also reveal the presence of bandgaps, which are the ranges of frequencies or wavelengths that cannot be transmitted by metamaterials.

Figure 3(a) shows the variations in the dispersion surfaces and curves for the free honeycomb metamaterial. It can be observed that this type of metamaterial had three dispersion surfaces. When $H = 0$, the two surfaces that were within the low-frequency range overlapped, and the structure had only

one bandgap, which was formed by the upper and middle surfaces. As the angular momentum increased, when $H = 1$, the overlap area between the middle and lower surfaces opened, resulting in the formation of a new bandgap. When H continued to increase to 5, the number of bandgaps in the system remained the same; however, the positions and bandwidths of each passband exhibited significant changes compared with $H = 1$. In summary, the increase in angular momentum not only introduced new bandgaps to the free metamaterial, but also significantly altered the position and range of each transmission band.
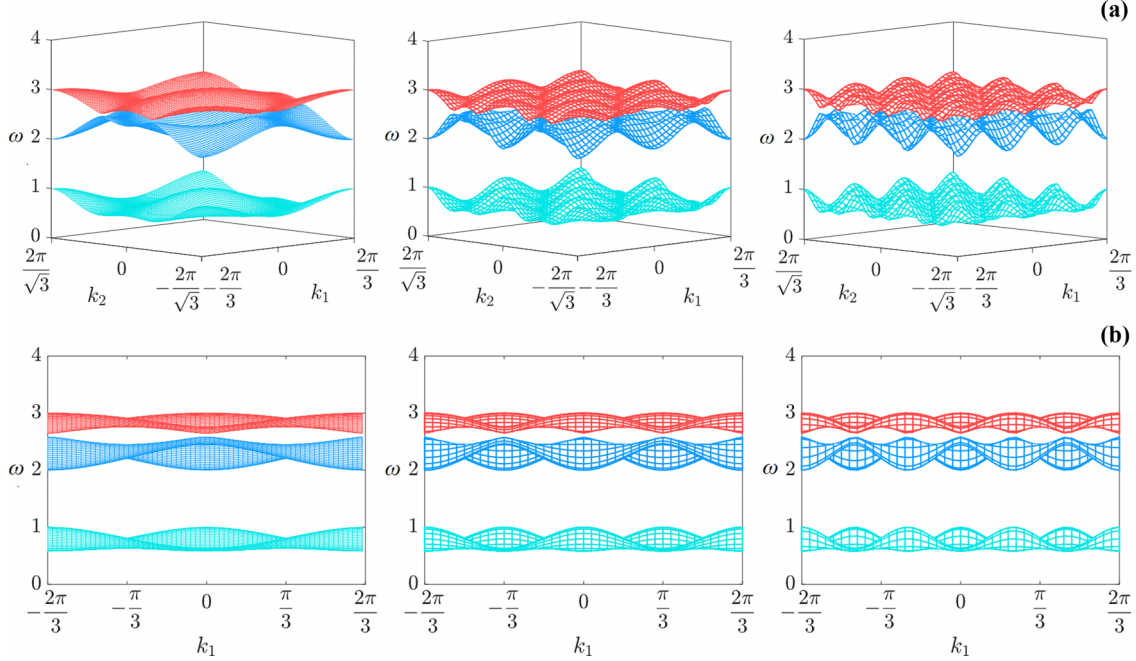
FIG. 4. The influence of spring dimensions on the dispersion surfaces of the constrained honeycomb metamaterials. (a) is the dispersion surface of the structure when $l = 1$, $l = 2$, and $l = 3$, and (b) is the corresponding frontal view.

Figure 3(b) shows the variation in the dispersion surfaces and curves of the constrained honeycomb metamaterial with respect to the speed of the gyroscope. In contrast to the free metamaterial, the constrained metamaterial did not have any bandgap when the gyroscope was static ($G = 0$), and bandgap characteristics only appeared when the gyroscope speed was introduced ($G = 2$). As G continued to increase ($G = 5$), the dispersion surfaces overlapped. In summary, for the constrained honeycomb metamaterial, an increase in G within a certain range increased the number of bandgaps in the system. However, exceeding this range resulted in a decrease in the number of bandgaps, whereas the bandwidth of each passband decreased with increasing G. This implies that an increase in G flattens the transmission bands.

Figure 4(a) shows the dispersion surfaces of the constrained honeycomb metamaterials for different spring dimensions, while Fig. 4(b) depicts the corresponding front views. It can be observed that as the dimensions increase, the width and range of the bandgap formed by the upper and middle surfaces does not change significantly. As shown in Fig. 2, changing the spring dimensions is equivalent to modifying the lattice size of the honeycomb lattice. Therefore, the lattice size has little effect on the width and range of the system bandgap.

B. Numerical verification of band structure

The band structure obtained above is the theoretical analytical result derived using the plane-wave expansion method. To verify its accuracy, numerical simulations can be performed by solving the original dynamic equations using the ODE45 function in MATLAB software. Taking the example of the constrained-type gyroscopic metamaterials with $G = 2$ and $l = 1$, the response of the structure to excitations of different frequencies was computed.

Figure 5 shows the relative positions of the excitation point and the observation point, as well as the dimensions of the numerical example structure. By solving Eq. (16), the overall response of the structure to the excitation can be obtained. The maximum displacement of the observation point within the observation time range can be identified. The ratio of this displacement to the excitation amplitude, defined as η, can characterize the propagation effect of the wave.

The amplitude-frequency response curves were plotted with the excitation frequency ω and the amplitude ratio η as the x and y coordinates, respectively, as shown in Fig. 6(b). It can be observed that significant wave propagation effects occur when ω is within the range of 0.6–1 and 2–3 rad/s. In contrast, for frequencies within other ranges, the wave propagation is almost negligible.

The comparative results between Figs. 6(a) and 6(b) demonstrate that the numerical calculations are in agreement with the band structure curves obtained through
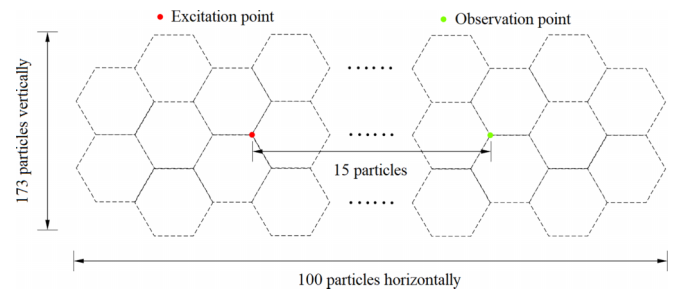

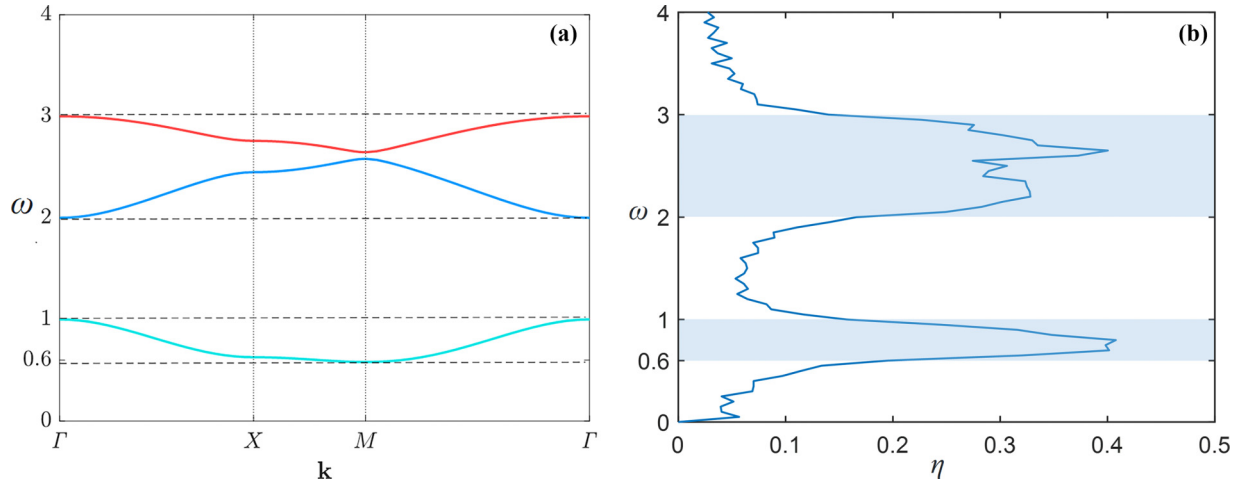FIG. 5. Schematic diagram of numerical verification model.

FIG. 6. (a) describes the dispersion relationships of constrained honeycomb metamaterials, when $G = 2$. (b) is the amplitude-frequency response curve.

theoretical analysis, thereby confirming the accuracy of the theoretical band gaps. This also indicates the ability of gyroscopic metamaterials to suppress vibrations and isolate noise.

C. Group-velocity analysis

Group velocity is another parameter analyzed in dispersion analysis. Analysis of group velocity can provide information on how waves are transmitted through a metamaterial and how they carry information. The group velocity is defined as a function of the wave number, and the normal direction of the dispersion surface contour corresponds to the direction of the group velocity of waves with this frequency.

The results shown in Fig. 7 indicate that when $H = 5$ and $G = 2$, the dispersion surfaces of the free and constrained metamaterials exhibited distinct characteristics in terms of the shape of their isofrequency contours. For the free metamaterial, as shown in Fig. 7(a), the isofrequency contours in the low-frequency region were nearly elliptical in shape, indicating the propagation of the wave in an elliptical form based on the definition of the group velocity. However, in the high-frequency region, the isofrequency contour on the lower surface gradually became quadrilateral in shape, whereas those on the middle and upper surfaces had a hexagonal shape, allowing the wave to propagate along the concentrated directions. Notably, there were four concentrated directions on the lower surface and six on the middle and upper surfaces. Figure 7(b) shows the isofrequency contours of the constrained metamaterial. The isofrequency contours were nearly circular in the low-frequency range, indicating that the waves propagated with equal intensity in all directions. In the high-frequency range, the contours assumed a hexagonal shape, and the waves exhibited six concentrated propagation directions that were similar among the three surfaces.

As waves propagate through a metamaterial, they interact with the unit structure. This interaction leads to different propagation directions and characteristics of waves with different frequencies in the metamaterial and also results in different

numbers of concentrating directions for different dispersion curves. This implies that metamaterials can optimally manipulate and process different signals, making them promising for a wide range of applications.

IV. NUMERICAL SIMULATION

Based on the analysis of the group-velocity direction described in the previous section, we explored the propagation direction and polarization characteristics of waves in the metamaterials using numerical simulations. Through this numerical simulation, we could better understand the response and processing capabilities of the metamaterials for different types of waves, which will promote the practical application of the metamaterials in various signal processing and manipulation applications.

A. Propagation properties of waves

Figure 8(a) shows the wave intensity response of a free-type gyroscopic metamaterial under positive circular displacement excitation, with the amplitude ratio of particle displacement to excitation represented by a gradient color. The results show that the propagation mode of the lower surface wave tended to become elliptical and exhibited a trend towards convergent propagation within certain frequency ranges. Two different excitation frequencies were applied to the middle surface, and it was found that under low-frequency excitation, the wave approximated an elliptical shape, whereas under high-frequency excitation, it exhibited a convergent propagation. The propagation characteristics of the upper surface were slightly different. Under low-frequency excitation, the waves appeared as convergent propagations, whereas under high-frequency excitation, the waveform approximated an elliptical propagation.

For the constrained gyroscopic metamaterial, distinct low- and high-frequency excitations were applied to the three dispersion surfaces. As shown in Fig. 8(b), by applying high and low excitation frequencies to each curved surface, the wave

FIG. 7. Contours of dispersion surfaces. (a) and (b) describe the contours of free and constrained honeycomb metamaterials, respectively, with assumptions that the angular momentum and gyroscope speed are $H = 5$ and $G = 2$, respectively.

propagation can be differentiated into circular and convergent propagations. Notably, in the adjacent dispersion surfaces, the wave propagation mode of the lower surface under high-frequency excitation was the same as that of the higher surface under low-frequency excitation. This indicates that although the bandgap caused by the rotation speed of the gyroscope isolated each passband, the propagation mode of the wave was continuous throughout the entire passband.

By simulating the response of the gyroid metamaterials to different excitations, it was verified that the direction of the elastic wave propagation was consistent with the direction revealed by the dispersion surface.

B. Polarization properties

As waveguide materials, phononic crystals prioritize the study of band structures over intrinsic frequencies. The differentiation of the dispersion surfaces in gyroid metamaterials and the differentiation of the intrinsic frequencies in gyroid structures are unified phenomena that yield different wave polarization modes, similar to the chiral modes in gyroid structures.

The polarization modes of waves on different dispersion surfaces can be solved using dynamic equations. However, the large number of equations in proportion to the number of
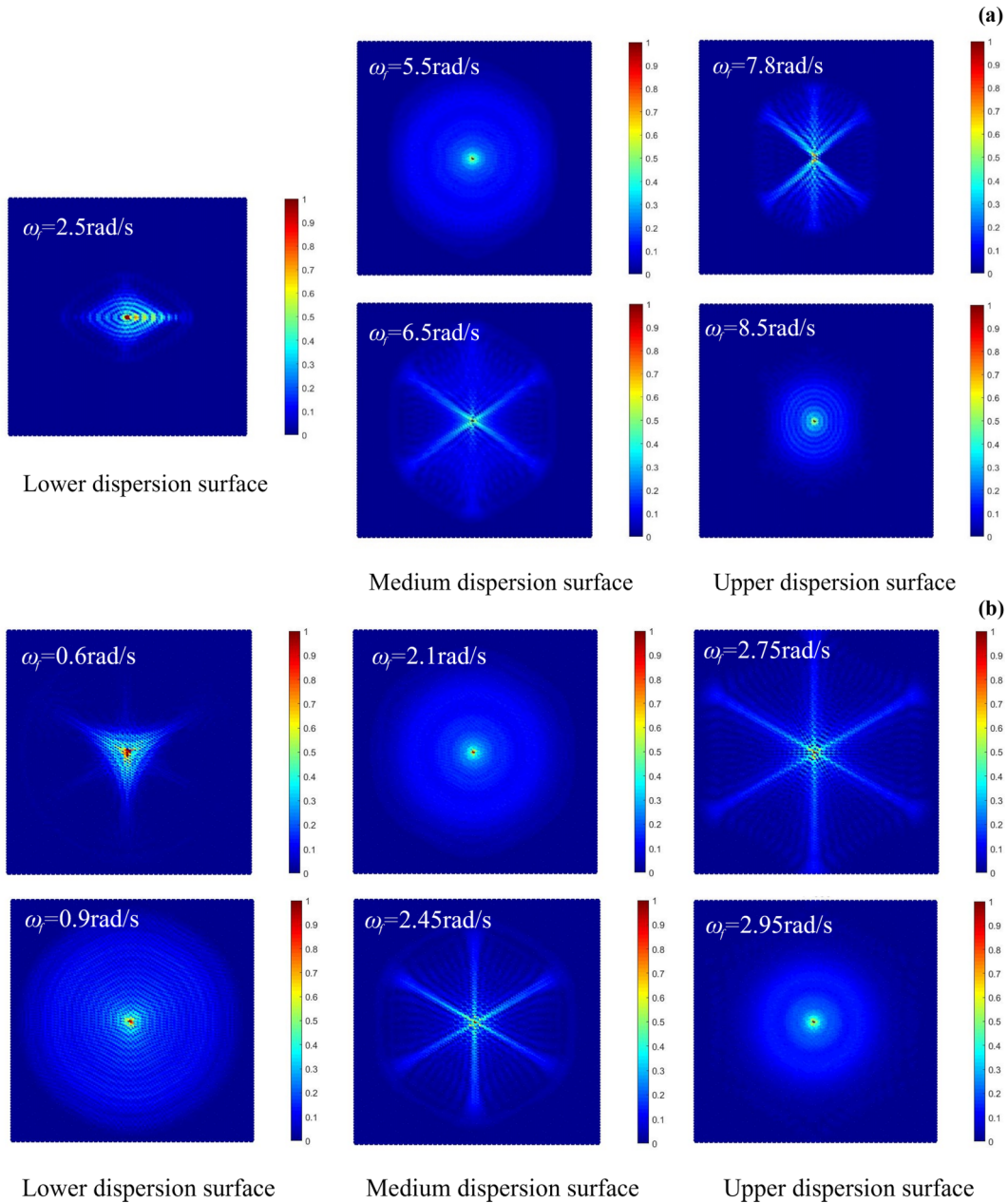
FIG. 8. Schematic of wave propagation. (a) and (b) correspond to free and constrained metamaterials, respectively, with an assumption that the angular momentum and gyroscope speed are $H = 5$ and $G = 2$, respectively. The top left corner of each figure is labeled with the respective circular excitation frequency ω_f.

cells in phononic crystals and their mutual coupling through elastic terms make the analytical solutions difficult to obtain. Therefore, the numerical solutions for the response of the structure to excitation can also be used to observe the different types of wave polarizations on different dispersion surfaces.

When applying forward and backward circular excitation to free-form metamaterials, the polarized waves are shown in Fig. 9(a). Both types of excitations induced forward waves in the structure of the lower-dispersion surface. However, different phenomena were observed for the middle- and upper-dispersion surfaces, where both types of excitation only induced backward waves. Therefore, free-form metamaterials exhibit a polarization effect in which waves can propagate re-

gardless of the type of excitation but with a specific polarized direction.

For the constrained metamaterials, as shown in Fig. 9(b), the lower surface exhibited backward polarization, whereas the middle and upper surfaces exhibited forward polarization and polarization effects.

Free-form and constrained metamaterials have similar structural symmetry; however, their different unit structures resulted in different polarization properties. The polarization properties of metamaterials can provide a better understanding of their microstructural properties, which can further facilitate in fine-tuning and exploring the performance and applications of the materials.

(a)

| Lower dispersion surface | Medium dispersion surface | Upper dispersion surface |

(b)

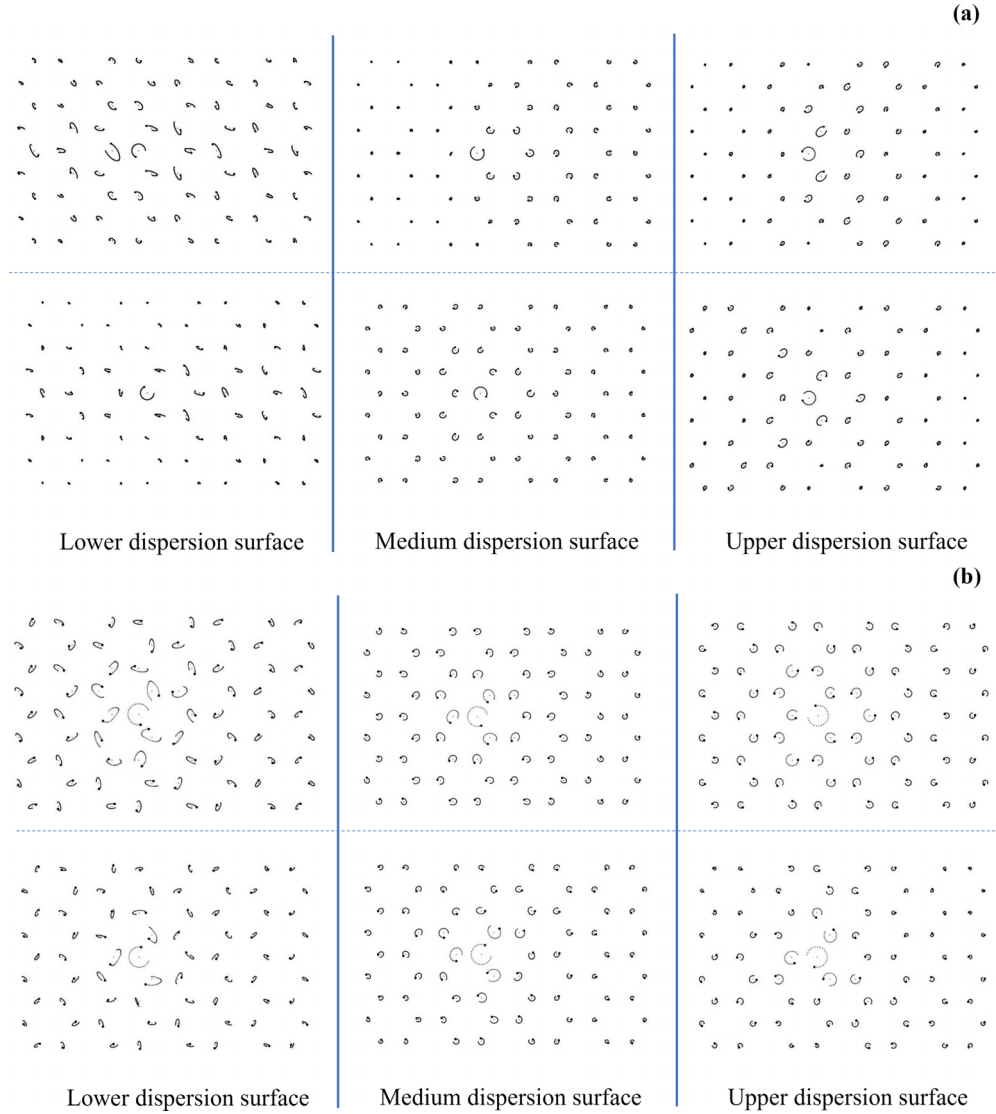| Lower dispersion surface | Medium dispersion surface | Upper dispersion surface |

FIG. 9. Response trajectories of excitation. (a) and (b) correspond to free and constrained metamaterials, respectively; the top row corresponds to positive circular excitation, whereas the bottom row corresponds to negative circular excitation, with an assumption that the angular momentum and gyroscope speed are $H = 5$ and $G = 2$, respectively. Counterclockwise rotation is defined as the positive direction, while clockwise rotation is considered the negative direction.

V. CONCLUSION

This study used two types of 2D honeycomb gyroid metamaterials: free and constrained. First, a dynamic modeling of the two structures was performed. Using the Bloch theorem, the dispersion relations of the systems were obtained, and the band structure characteristics were theoretically analyzed. Finally, numerical simulations were performed to thoroughly investigate the wave propagation and polarization properties of the systems. The main findings are summarized as follows:

(1) Increasing the rotation speed of the gyroscope flattened the original dispersion surfaces and separated them from each other, resulting in bandgaps. Gyroscopes suppress vibrations by controlling the energy band of metamaterials based on this theory.

(2) The wave group-velocity directions of the two types of structural dispersion surfaces alternated between isotropic and concentrated in certain directions under different frequency excitations. Numerical simulations verified the accuracy of the theoretically obtained bandgaps and group-velocity directions.

(3) Through numerical computations, it was discovered that honeycomb gyroscopic metamaterials exhibit polarization characteristics. Specifically, regardless of the excitation method used, if the energy is inputted within the passband frequency range, the corresponding polarized wave output can be obtained. Therefore, honeycomb gyroscopic metamaterials can be used as polarization devices.

APPENDIX A

The **N** matrix in Eq. (7) can be expressed as

$$
\mathbf{N} = \begin{bmatrix} N_{11} & N_{12} & N_{13} & N_{14} \\ N_{21} & N_{22} & N_{23} & N_{24} \\ N_{31} & N_{32} & N_{33} & N_{34} \\ N_{41} & N_{42} & N_{43} & N_{44} \end{bmatrix},
$$

where

$$
N_{11} = I\omega^2 - \frac{3}{2}c_1 - \frac{3}{2}c_2
$$

$$
N_{12} = c_1\left(1 + \frac{1}{4}e^{-\alpha}e^{-\beta} + \frac{1}{4}e^{-\alpha}e^{\beta}\right)
$$
$$
+ c_2\left(\frac{3}{4}e^{-\alpha}e^{-\beta} + \frac{3}{4}e^{-\alpha}e^{\beta}\right)
$$

$$
N_{13} = Hi\omega - \frac{\sqrt{3}}{2}c_1 - \frac{\sqrt{3}}{2}c_2
$$

$$
N_{14} = c_1\left(\frac{\sqrt{3}}{4}e^{-\alpha}e^{-\beta} + \frac{\sqrt{3}}{4}e^{-\alpha}e^{\beta}\right)
$$
$$
+ c_2\left(\frac{\sqrt{3}}{4}e^{-\alpha}e^{-\beta} + \frac{\sqrt{3}}{4}e^{-\alpha}e^{\beta}\right)
$$

$$
N_{21} = -Hi\omega - \frac{\sqrt{3}}{2}c_1 - \frac{\sqrt{3}}{2}c_2,
$$

$$
N_{22} = c_1\left(\frac{\sqrt{3}}{4}e^{-\alpha}e^{-\beta} + \frac{\sqrt{3}}{4}e^{-\alpha}e^{\beta}\right)
$$
$$
+ c_2\left(\frac{\sqrt{3}}{4}e^{-\alpha}e^{-\beta} + \frac{\sqrt{3}}{4}e^{-\alpha}e^{\beta}\right)
$$

$$
N_{23} = I\omega^2 - \frac{3}{2}c_1 - \frac{3}{2}c_2
$$

$$
N_{24} = c_1\left(\frac{3}{4}e^{-\alpha}e^{-\beta} + \frac{3}{4}e^{-\alpha}e^{\beta}\right)
$$
$$
+ c_2\left(1 + \frac{1}{4}e^{-\alpha}e^{-\beta} + \frac{1}{4}e^{-\alpha}e^{\beta}\right)
$$

$$
N_{31} = c_1\left(1 + \frac{1}{4}e^{\alpha}e^{\beta} + \frac{1}{4}e^{\alpha}e^{-\beta}\right) + c_2\left(\frac{3}{4}e^{\alpha}e^{\beta} + \frac{3}{4}e^{\alpha}e^{-\beta}\right)
$$

$$
N_{32} = I\omega^2 - \frac{3}{2}c_1 - \frac{3}{2}c_2
$$

$$
N_{33} = c_1\left(\frac{\sqrt{3}}{4}e^{\alpha}e^{\beta} + \frac{\sqrt{3}}{4}e^{\alpha}e^{-\beta}\right)
$$
$$
+ c_2\left(\frac{\sqrt{3}}{4}e^{\alpha}e^{\beta} + \frac{\sqrt{3}}{4}e^{\alpha}e^{-\beta}\right)
$$

$$
N_{34} = Hi\omega - \frac{\sqrt{3}}{2}c_1 - \frac{\sqrt{3}}{2}c_2
$$

$$
N_{41} = c_1\left(\frac{\sqrt{3}}{4}e^{\alpha}e^{\beta} + \frac{\sqrt{3}}{4}e^{\alpha}e^{-\beta}\right)
$$
$$
+ c_2\left(\frac{\sqrt{3}}{4}e^{\alpha}e^{\beta} + \frac{\sqrt{3}}{4}e^{\alpha}e^{-\beta}\right)
$$

$$
N_{42} = -Hi\omega - \frac{\sqrt{3}}{2}c_1 - \frac{\sqrt{3}}{2}c_2
$$

$$
N_{43} = c_1\left(1 + \frac{1}{4}e^{\alpha}e^{\beta} + \frac{1}{4}e^{\alpha}e^{-\beta}\right) + c_2\left(\frac{3}{4}e^{\alpha}e^{\beta} + \frac{3}{4}e^{\alpha}e^{-\beta}\right)
$$

$$
N_{44} = I\omega^2 - \frac{3}{2}c_1 - \frac{3}{2}c_2,
$$

and

$$
\alpha = i3k_1l/2, \ \beta = i\sqrt{3}k_2l/3.
$$

APPENDIX B

The **M**, **G**, and **C** matrices in Eq. (18) can be expressed, respectively as

$$
\mathbf{M} = m\mathbf{I},
$$

$$
\mathbf{G} = iG\begin{pmatrix} 0 & 1 & 0 & 0 \\ -1 & 0 & 0 & 0 \\ 0 & 0 & 0 & 1 \\ 0 & 0 & -1 & 0 \end{pmatrix},
$$

$$
\mathbf{C} = c\begin{pmatrix} \frac{3}{2} & 0 & -1 - \frac{e^{-i\alpha}+e^{-i\beta}}{4} & \frac{\sqrt{3}(e^{-i\alpha}-e^{-i\beta})}{4} \\ 0 & \frac{3}{2} & \frac{\sqrt{3}(e^{-i\alpha}-e^{-i\beta})}{4} & -\frac{3(e^{-i\alpha}+e^{-i\beta})}{4} \\ -1 - \frac{e^{i\alpha}+e^{i\beta}}{4} & \frac{\sqrt{3}(e^{i\alpha}-e^{i\beta})}{4} & \frac{3}{2} & 0 \\ \frac{\sqrt{3}(e^{i\alpha}-e^{i\beta})}{4} & -\frac{3(e^{i\alpha}+e^{i\beta})}{4} & 0 & \frac{3}{2} \end{pmatrix},
$$

where

$$
\alpha = (3k_1 - \sqrt{3}k_2)l/2, \ \beta = (3k_1 + \sqrt{3}k_2)l/2.
$$

[1] M. M. Sigalas and E. N. Economou, Elastic and acoustic wave band structure, J. Sound Vib. **158**, 377 (1992).

[2] Z. Y. Liu, X. X. Zhang, Y. W. Mao, Y. Y. Zhu, Z. Y. Yang, C. T. Chan, and P. Sheng, Locally resonant sonic materials, Science **289**, 1734 (2000).

[3] T. Kan, A. Isozaki, N. Kanda, N. Nemoto, K. Konishi, M. Kuwata-Gonokami, K. Matsumoto, and I. Shimoyama, Spiral metamaterial for active tuning of optical activity, Appl. Phys. Lett. **102**, 221906 (2013).

[4] K. Wang, J. X. Zhou, C. Q. Cai, D. L. Xu, and H. J. Ouyang, Mathematical modeling and analysis of a meta-plate for very low-frequency band gap, Appl. Math. Modell. **73**, 581 (2019).

[5] S. X. Yang, J. H. Page, Z. Y. Liu, M. L. Cowan, C. T. Chan, and P. Sheng, Focusing of sound in a 3D phononic crystal, Phys. Rev. Lett. **93**, 024301 (2004).

[6] M. I. Hussein, M. J. Leamy, and M. Ruzzene, Dynamics of phononic materials and structures: Historical origins, recent progress, and future outlook, Appl. Mech. Rev. **66**, 040802 (2014).

[7] T. Vasileiadis, J. Varghese, V. Babacic, J. Gomis-Bresco, D. Navarro Urrios, and B. Graczykowski, Progress and perspectives on phononic crystals, J. Appl. Phys. **129**, 160901 (2021).

[8] W. J. Zhou, Z. Y. Chen, Y. J. Chen, W. Q. Chen, C. W. Lim, and J. N. Reddy, Mathematical modelling of phononic nanoplate and its size-dependent dispersion and topological properties, Appl. Math. Modell. **88**, 774 (2020).

[9] J. Hwan Oh, I. Kyu Lee, P. Sik Ma, and Y. Young Kim, Active wave-guiding of piezoelectric phononic crystals, Appl. Phys. Lett. **99**, 083505 (2011).

[10] Y. Yuan, J. Li, R. H. Bao, and W. Q. Chen, A double-layer metastructured beam with contact-separation switchability, Mech. Adv. Mater. Struct. **29**, 1011 (2020).

[11] B. Li, C. Zhang, F. Peng, W. Z. Wang, B. D. Vogt, and K. T. Tan, 4D printed shape memory metamaterial for vibration bandgap switching and active elastic-wave guiding, J. Mater. Chem. C **9**, 1164 (2021).

[12] J. Li and C. T. Chan, Double-negative acoustic metamaterial, Phys. Rev. E **70**, 055602(R) (2004).

[13] P. F. Pai, H. Peng, and S. Y. Jiang, Acoustic metamaterial beams based on multi-frequency vibration absorbers, Int. J. Mech. Sci. **79**, 195 (2014).

[14] X. D. Yang, Q. D. Cui, Y. J. Qian, W. Zhang, and C. W. Lim, Modulating band gap structure by parametric excitations, J. Appl. Mech. **85**, 061012 (2018).

[15] S. Park, R. Horowitz, and C.-W. Tan, Dynamics and control of a MEMS angle measuring gyroscope, Sens. Actuators A **144**, 56 (2008).

[16] T. Sasaki, T. Shimomura, S. Pullen, and H. Schaub, Attitude and vibration control with double-gimbal variable-speed control moment gyros, Acta Astronaut. **152**, 740 (2018).

[17] M. Lungu, Neuro-observer based control of double gimbal control moment gyro systems, Aerosp. Sci. Technol. **110**, 106467 (2021).

[18] Q. Hu, Y. H. Jia, and S. J. Xu, Dynamics and vibration suppression of space structures with control moment gyroscopes, Acta Astronaut. **96**, 232 (2014).

[19] X. Feng, Y. H. Jia, and S. J. Xu, Dynamics of flexible multibody systems with variable-speed control moment gyroscopes, Aerosp. Sci. Technol. **79**, 554 (2018).

[20] Q. Luo, D. X. Li, and J. P. Jiang, Coupled dynamic analysis of a single gimbal control moment gyro cluster integrated with an isolation system, J. Sound Vib. **333**, 345 (2014).

[21] M. Attarzadeh, S. Maleki, J. L. Crassidis, and M. Nouh, Non-reciprocal wave phenomena in energy self-reliant gyric metamaterials, J. Acoust. Soc. Am. **146**, 789 (2019).

[22] A. Baz, Active synthesis of a gyroscopic-nonreciprocal acoustic metamaterial, J. Acoust. Soc. Am. **148**, 1271 (2020).

[23] L. Y. Yao, G. Q. Jiang, F. Wu, and J. Y. Luo, Band structure computation of two-dimensional and three-dimensional phononic crystals using a finite element-least square point interpolation method, Appl. Math. Modell. **76**, 591 (2019).

[24] C. He, S. H. Zhou, and P. J. Guo, Mitigation of railway-induced vibrations by using periodic wave impeding barriers, Appl. Math. Modell. **105**, 496 (2022).

[25] O. Toader and S. John, Proposed square spiral microfabrication architecture for large three-dimensional photonic band gap crystals, Science **292**, 1133 (2001).

[26] M. Brun, I. S. Jones, and A. B. Movchan, Vortex-type elastic structured media and dynamic shielding, Proc. R. Soc. A **468**, 3027 (2012).

[27] X. M. Zhou and Y. C. Zhao, Unusual one-way edge state in acoustic gyroscopic continuum, Sci. China Phys., Mech. Astron. **62**, 14612 (2019).

[28] P. Wang, L. Lu, and K. Bertoldi, Topological phononic crystals with one-way elastic edge waves, Phys. Rev. Lett. **115**, 104302 (2015).

[29] L. M. Nash, D. Kleckner, A. Read, and W. T. M. Irvine, Topological mechanics of gyroscopic metamaterials, Proc. Natl. Acad. Sci. USA **112**, 14495 (2015).